Yubing Zhang
Yong Wang
Guang Sun
Jiazhen Han
Yudong Xie

http://dx.doi.org/10.21278/brod73106

ISSN 0007-215X
eISSN 1845-5859

EFFECTS OF TWO TYPES OF CONTROLLABLE DEFORMATION ON ENERGY EXTRACTION OF A FLEXIBLE HYDROFOIL

UDC 551.46.09
Original scientific paper

Summary

Energy extraction capacity of controllably flexible hydrofoil was studied under two identified deformation modes. Deformation modes, flexure parameters (flexure amplitude α and flexure coefficient β) and motion parameters (reduced frequency f^* and pitching amplitude θ_0) were investigated to understand the effects of controllably flexible deformation on energy extraction. The results reveal that deformation modes affect the effective angle of attack and vortex structure, which influence hydrodynamic performance. The energy extraction capacity improves from the deformation mode 2 to the rigid hydrofoil and then to the deformation mode 1. Under the deformation mode 1, lift, moment and power coefficients are increased obviously with the increase of α, while they increase slightly with β. Power coefficients and efficiency are sensitive to α, which influences the development of leading-edge vortices. The flexible coefficient β affects the wake structure, which has less impact on variation of force coefficient. As the increase in f^*, averaged power coefficients firstly increase and then decrease. Further, the optimal f^* is subjected to θ_0. Interestingly, a critical reduced frequency f^*_s, which is generally increase with increasing θ_0, was found under three modes. The condition that $f^* > f^*_s$. is a prerequisite for subsequent adjustments of flexure modes and parameters according to different requirement of power coefficient under different tidal currents. The range of high efficiency (η) is: deformation mode 1 ($36.1\% < \eta < 54.3\%$) > rigid hydrofoils ($34.2\% < \eta < 41\%$) > deformation mode 2 ($26.9\% < \eta < 30.3\%$).

Key words: *Tidal energy; Oscillating hydrofoil; Hydrodynamic; Flexible hydrofoil*

1. Introduction

With fossil fuel consumption, energy and environmental crisis have become great challenges to the world. Renewable energy such as wind, solar energy and ocean energy, which are resource-rich and clean, have been maintaining a steady progress. Tidal current

energy, as one of ocean energy, has been attracting tremendous attentions owning to its high energy density and predictability. Generally, it can be extracted through blades rotation such as horizonal and vertical-axis turbines [1]. Inspired by insect flight, energy can be extracted by oscillating motions. The concept of oscillating movement was proposed by McKinney and DeLaurier [2]. Their results indicated that the efficiency of oscillating wings employed with pitching and plunging motions was comparable to that of rotating blades. In recent decades, the uses of oscillating hydrofoils as energy harvesters have received much attention due to more environmentally friendly compared with rotating blades [3]. What's more, oscillating hydrofoil turbines are well-suited to shallow water sites [4], which further maximizes the utility of marine space.

Kinematic motion parameters of oscillating hydrofoils are well known as key factors to improve power extraction efficiency. Many researchers have devoted to improving power extraction efficiency through parameter optimization involved (heaving amplitude, pitching amplitude, reduced frequency, phase shift and pitching axis location) [2, 3, 5-9]. Kinsey et al. observed that combined heave-pitch motion could extract energy and the maximum efficiency could go up to 34% [5]. Power extraction efficiency is vary with different motion amplitudes and the maximum efficiency reached about 43% when heaving amplitude/chord is in the range of 1-2 [9]. Zhu and Peng found that the pitching axis location near pressure center could decrease power consumption, thus optimal performance is achieved [6]. Non-sinusoidal flapping motions have also been studied to get a better energy harvesting performance [10, 11]. Ashraf et al. demonstrated that the power and efficiency of an oscillating wing with non-sinusoidal pitch-plunge motion improved about 17% and 15%, respectively, compared with that of sinusoidal motion [12]. Xie et al. found that high reduce frequency combined with low pitching angle is beneficial to energy extraction [13]. Dual foils or multi-foil array configuration exhibit superior energy extraction compared with one foil. Ma et al. carried out the analysis of dual oscillating foils [14, 15]. Extensive works have also been conducted by Karbasian et al. [16], Xu et al. [17], and Kim et al. [18].

Oscillating hydrofoils with a swing arm was also investigated [19]. Sitorus and Ko found that left-swing types exhibits better hydrodynamic performance due to the good synchronization of forces with translational velocity as well as moment and pitch angular rate [20]. The hydrokinetic performance of a flapping foil under the swing arm mode is higher than that of simple heaving-pitching mode [21]. The peak efficiency of 0.21 is obtained when the swing factor is 0.25. Lahooti et al. found that the heaving force and pitching moment could be improved significantly under suitable conditions [22]. Ma et al. investigated the effect of unsteady currents on power extraction of oscillating foils and they reported that the total efficiency was slightly affected at a lengthy period [23]. Wang et al. numerically investigated the influences of different series foil shapes on the power extraction of flapping hydrofoils [24].

The above studies mainly base on rigid hydrofoils. However, the flexible feature of fins and wings indicates that compared with rigid foils, flexible foil certainly has some merits. Researches on flexible wings in initial stages mainly focus on the reinforcement of thrust performance and propulsion efficiency [25]. Zhu reported that the efficiency could be improved through the chordwise flexing [26]. Tay and Lim found from their numerical study that the average thrust coefficient could reach to 3.57 [27].

Recently, the power extraction capacity of oscillating hydrofoils with flexure deformation has aroused the interest of researchers due to superior hydrodynamic performance [28]. Tian et al. achieved a power coefficient of 38.2% [29]. Liu et al. investigated the influences of passive flexibility on the efficiency of a flapping foil [30]. Le et al. demonstrated that efficiency improved 30% and 15% under 2D and 3D simulations, respectively [31]. The pressure difference between upper and lower surface of the foil could

be improved by a flexible tail, thus improving the power extraction efficiency [32, 33]. The leading and trailing edge deformation increase the camber of deforming foil surfaces, which could improve the energy harvesting efficiency [34, 35].

As mentioned in the literature [31], the chordwise flexibility of hydrofoils affects the pressure distribution, vortices formation and shedding time scales, which directly affects the hydrodynamic characteristics of hydrofoils. Tidal current conditions are complex and changeable. By controlling the flexible wing to deform reasonably respect to flow velocity conditions, the power extraction efficiency could be improved, which could expand the application range of tidal current energy. In other words, the optimal power and efficiency could be obtained by reasonable deformation of hydrofoils in places with high or low flow rate. To the knowledge of authors, there are few works about flexible hydrofoils and little research referring to the influences of flexure parameters on power extraction performance. In addition, systematic analysis for effects of flexibility under different motion parameters on power extraction has not been well developed yet and need to be further investigated.

Zhu et al. found that the energy extraction efficiency could be improved by the active synchronous arc deformation and in their study both leading and trailing edges were deformable [36]. However, in this study, the part from leading edge to pitching axis is rigid, and the rest is flexible. By tuning the adjustable parameters of the flexible amplitude α and flexible coefficient β, the shapes of upper and lower surfaces of hydrofoils can gradually change corresponding to the change of chord line. In addition, deformation modes, flexure parameters and a wide range of kinematic parameters are studied. A comprehensive study is conducted in terms of force coefficients, effective angle of attack, vortices structures, and power extraction capabilities. Furthermore, the appropriate range of parameters is presented and the evolutions of pressure distribution are also discussed.

2. Computational approach

2.1. Numerical method

In this study, unsteady incompressible viscous flows around an oscillating hydrofoil are governed by equations as follows:

$$\frac{\partial u_x}{\partial x}+\frac{\partial u_y}{\partial y}=0 \tag{1}$$

$$\frac{\partial u_x}{\partial t}+u_x\frac{\partial u_x}{\partial x}+u_y\frac{\partial u_x}{\partial y}=F_x-\frac{1}{\rho}\frac{\partial p}{\partial x}+\nu\nabla^2 u_x \tag{2}$$

$$\frac{\partial u_y}{\partial t}+u_x\frac{\partial u_y}{\partial x}+u_y\frac{\partial u_y}{\partial y}=F_y-\frac{1}{\rho}\frac{\partial p}{\partial y}+\nu\nabla^2 u_y \tag{3}$$

where p, v and ρ are the pressure, viscosity and density, respectively; u_x and F_x denote the velocity and force in x direction; u_y and F_y denote the velocity and force in y direction.

Spalart-Allmaras turbulence model was selected for simulations [5, 37]. Pressure Implicit with Splitting of Operator algorithm was employed. In addition, the movement and deformation of hydrofoils was controlled by User defined function (UDF). The pressure discretization is second order scheme. Momentum and modified turbulent viscosity discretization are second order upwind schemes. Absolute convergence criteria was 10^{-5} in the present study. Power coefficients and force coefficients are determined after six cycles in order to ensure the stable convergence computations.

A mesh model is established for simulation, as shown in Fig. 1. The square fluid

computational domain is 75c × 75c and the center is the pitching axis location of hydrofoils. The mesh is composed of three sub-domains. The external-domain (red) and middle-domain (blue) are connected with a sliding interface. The interface ensures that the external-domain only has a heaving movement. In addition, the middle-domain experiences a synchronous heaving/pitching movement. It must be noted that the grid of middle-domain is only moved as a whole grid, which means that it is not re-meshed. However, the grid of internal-domain (green) is re-meshed due to the deformation of hydrofoils. Quadrilateral cells are used for boundary layers. In order to ensure the accuracy of deformation motion, a fine mesh of the internal-domain is created. The internal-domain experiences a synchronous heaving/pitching/deforming motion, which avoids grid distortion and ensures minimum effects of grid deformation on simulations.

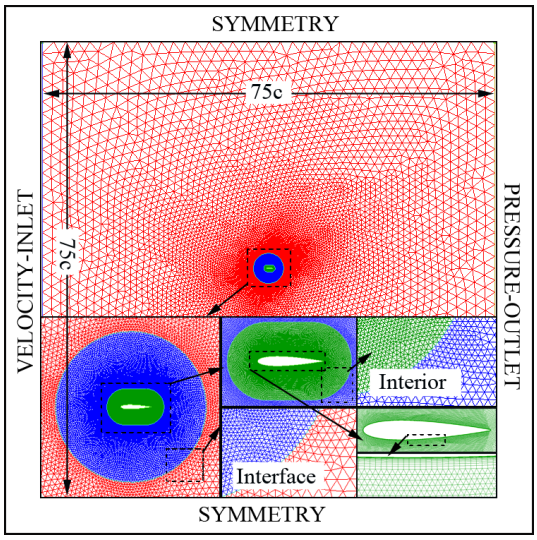

Fig. 1 Grid details and boundary conditions

2.2. Kinematic motion profile of hydrofoils

Fig. 2(a)-(c) show the down-stroke of the rigid hydrofoil, deformation mode 1 and deformation mode 2, respectively. And the up-stroke is the reversed process, thus no display here. The research focus in this work is the effect of flexure of hydrofoils on power extraction performance, thus, the traditional periodic motions of hydrofoils are adopted. And following equations express the heaving and pitching motion pattern:

$$h(t) = h_0 \sin(2\pi ft + \varphi) \tag{4}$$

$$\theta(t) = \theta_0 \sin(2\pi ft) \tag{5}$$

$$\dot{h}(t) = \frac{dh(t)}{dt} \tag{6}$$

$$\dot{\theta}(t) = \frac{d\theta(t)}{dt} \tag{7}$$

where $\dot{h}(t)$ and $\dot{\theta}(t)$ are the heaving velocity and pitching angular velocity, respectively; h_0 and θ_0 are the heaving and pitching amplitude respectively; f is the frequency; φ is the phase difference between heaving and pitching motion. The chord length c is 0.25m; the heaving amplitude h_0/c is 1; the pitching axis location is c/3 from the leading edge. The phase difference φ is kept at 90°; the flow velocity U_∞ is 2m/s; the reduced frequency determined as

$f^*=fc/U_\infty$; the Reynolds number (R_e) determined as $R_e= cU_\infty/\nu$ is 5×10^5, where ν is the viscosity of seawater.

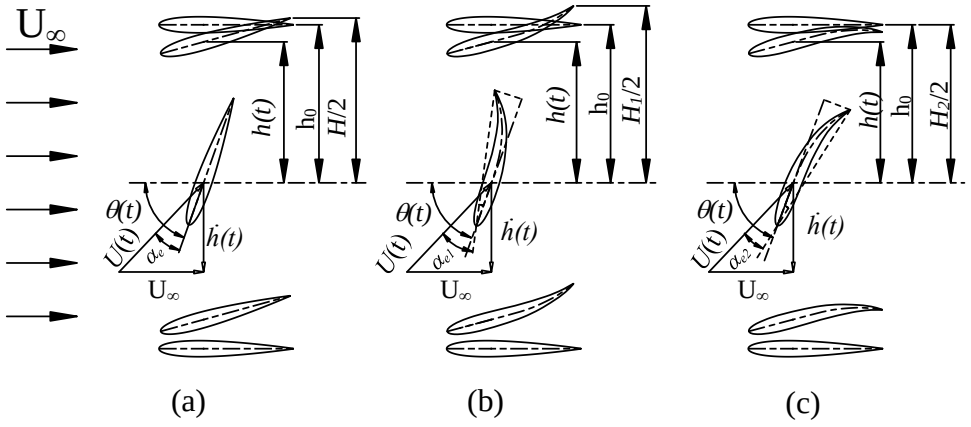

(a) (b) (c)

Fig. 2 Schematics of oscillating hydrofoil motion during down-stroke phases: (a)rigid hydrofoil; (b) deformation mode 1; and (c) deformation mode 2

On the basis of Bose's chordwise deformation theory [38], a modified flexure model is proposed and the chordwise flexure deformation f(x, t) can be described by the following function:

$$f(x,t)=(\delta/2^{\beta})[(3x/2c)^2+(3x/2c)^3]^{\beta}\sin(2\pi ft+\phi) \tag{8}$$

$$\alpha=\delta/c \tag{9}$$

where c is the chord length; x is the coordinate value of cells of hydrofoil thread in relative coordinate system. It must be noted that the value of x is determined in relative coordinate system, in which the hydrofoil only occurs deformation motion. The relative coordinate system performs the combined heaving/pitching motion in global coordinate system. The part from trailing edge to pitching axis is flexible, and the rest is rigid. δ is the flexure amplitude, denoting the maximum deformation value of trailing edge tips. A dimensionless parameter α, which is determined as $\alpha=\delta$/c, is used. β is the flexure coefficient, denoting the curvature of chord line. These various meaning is discussed in the following paragraph. ϕ is the phase difference of flexure deformation direction, and 0 refers to the deformation mode 1 and π refers to the deformation 2.

Le and Ko [31] demonstrated that power extraction efficiency improved 30% when the chordwise flexure is 20%. Different from their research, this study focuses on the different β under the variation of α. In other words, the different β denotes the different curvature shapes under the same α. Fig. 3(a) displays the deformation mode 1 during down-stroke at t/T=0.25, which is consistent with Fig. 2(b). Fig. 3(b) displays the deformation mode 2 during down-stroke at t/T=0.25, which is consistent with Fig. 2(c).

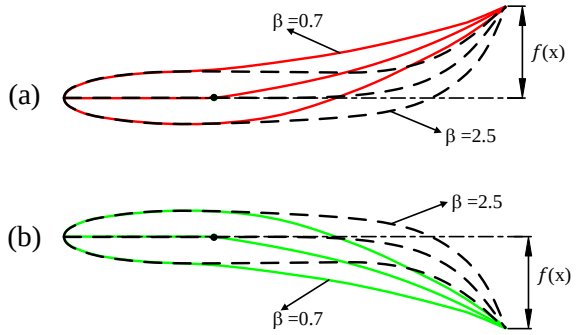

Fig. 3 Schematics of the flexible hydrofoil with two different deformation patterns at α=20%: (a) deformation mode 1; and (b) deformation mode 2

2.3. Power extraction parameters

The lift coefficients (C_y), drag coefficients (C_x) and moment coefficient (C_m) were obtained by the following equations:

$$C_y = F_y / 0.5\rho U_\infty^2 cb \tag{10}$$

$$C_x = F_x / 0.5\rho U_\infty^2 cb \tag{11}$$

$$C_m = F_m / 0.5\rho U_\infty^2 c^2 b \tag{12}$$

where F_y is the lift force; F_x is the drag force; F_m is the moment; and b is the span length, which is equal to one unit length for 2D model.

A vertical linear velocity ($\dot{h}(t)$), which is caused by the heaving motion of hydrofoils, results in that the instantaneous equivalent inflow velocity is not the flow velocity (U_∞), which can be seen in Fig. 2. The equivalent inflow velocity ($U(t)$) can be determined as:

$$U(t) = \sqrt{(U_\infty^2 + \dot{h}(t)^2)} \tag{13}$$

The effective angle of attack is the interior angle between the line from the leading edge to the trailing edge tips [34] and $U(t)$, as shown in Fig. 2. In other words, the angle is the combination of the velocity induced, pitching angles and flexible deformation. The angle induced by the flexure of hydrofoils cannot be ignored. Therefore, the effective angle of attack of rigid hydrofoils (α_e), deformation mode 1 (α_{e1}) and deformation mode 2 (α_{e2}) can be expressed as:

$$\alpha_e = -arctan(-\dot{h}(t)/U_\infty) + \theta(t) \tag{14}$$

$$\alpha_{e1} = -arctan(-\dot{h}(t)/U_\infty) + \theta(t) + arctan(f(t)/c) \tag{15}$$

$$\alpha_{e2} = -arctan(-\dot{h}(t)/U_\infty) + \theta(t) + arctan(f(t)/c) \tag{16}$$

where f(t) is the flexible deformation of trailing edge tips.

The instantaneous power coefficient $C_p(t)$, averaged power coefficient $\bar{C}_p$ and efficiency (η) can be can be written as:

$$C_P(t) = P(t)/0.5\rho U_\infty^3 c = 2[F_y\dot{h}(t) + F_m\dot{\theta}(t)]/\rho U_\infty^3 c \tag{17}$$

$$P(t) = F_y\dot{h}(t) + F_m\dot{\theta}(t) \tag{18}$$

$$\overline{C}_P = (1/T)\int_t^{t+T} C_P(t)dt \tag{19}$$

$$\eta = 0.5\rho U_\infty^3 cb\overline{C}_P / 0.5\rho U_\infty^3 Hb = \overline{C}_P c / H \tag{20}$$

where *P(t)* is the instantaneous power. It must be noted that the instantaneous power consists of two components: heaving motion power ($F_y\dot{h}(t)$) and pitching motion power ($F_m\dot{\theta}(t)$) [31].The user defined function (UDF) was used to calculate the force and velocity [4, 15, 19]. The force of the hydrofoil thread unit is extracted through UDF, and the force of the grid unit is added up to be the total force. *H* is the rigid foil's swept distance. H_1 and H_2 are the swept distance of deformation mode 1 and deformation mode 2, respectively, as shown in Fig. 2.

2.4 The independence validation of grid number and time step

In this section the tests were done under deformation mode 1 in h_0/c=0.5, θ_0=80°, f*=0.1, α=8% and β=1. Fig. 4 shows C_y for the different cases during one cycle. It can be seen that the results are gradually converged with grid number increase and time step size decrease. Table. 1 shows $\overline{C}_p$ and its error in one cycle. The errors are determined based on the case 7. As shown in table. 1, the errors of case 6 is 1.3%, which within 3%. It can be concluded that at this level the influences of grid number and time step are very limited and can be reasonably ignored. Therefore, in this study, a number of 1.21×10^5 cells and 1600 ts/cycle are chosen for all simulations.

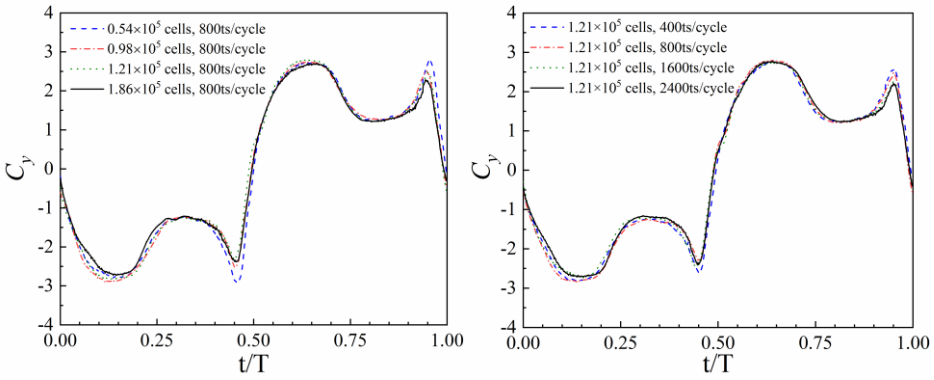

Fig. 4 The instantaneous lift coefficients during one cycle

Table 1 The averaged power coefficient ($\overline{C}_p$) and its error during one cycle.

Case	Number of grids	Time steps/T	$\overline{C}_p$	error%
Case 1	0.54×10^5	800	1.018	10.5
Case 2	0.98×10^5	800	0.989	7.3
Case 3	1.21×10^5	800	0.954	3.6
Case 4	1.86×10^5	800	0.951	3.3
Case 5	1.21×10^5	400	0.968	5.1
Case 6	1.21×10^5	1600	0.933	1.3
Case 7	1.21×10^5	2400	0.921	---

3. Results and discussions

3.1. Validation study

The reliability of code settings and iteration schemes of software have been validated in our previous works [14, 15, 23, 39]. To further validate the present code settings for

oscillating hydrofoils, the comparisons have been made with the simulation results from Kinsey and Dumas [4]. Their simulation results were compared with prototype experiments. Fig. 5 exhibits that C_y and C_x in present study show good agreement with that of Kinsey and Dumas [4]. Therefore, it can be revealed that the code parameter settings and iteration scheme in this study are correctness.

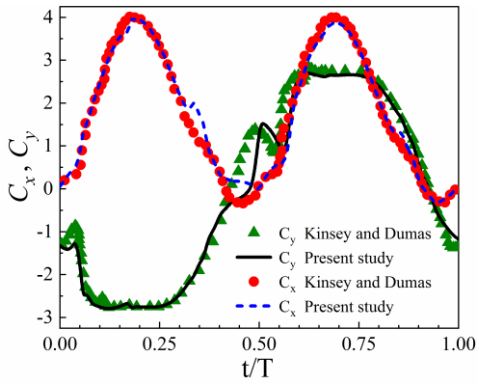

Fig. 5 C_y and C_x between reference and present simulation

3.2. Influences of α and β on hydrodynamics

In this section, tests were done under the deformation mode 1 in f^*=0.1, θ_0=60°, α=5%-20% and β=0.7-2.5. Instantaneous force and power coefficients are reviewed and compared with rigid hydrofoils during one cycle for sufficient examinations.

To quantify the influence of α and β on hydrodynamic of an oscillating hydrofoil, the averaged power coefficient ($\bar{C}_p$) and efficiency (η) are computed and listed in Table. 2. $\bar{C}_p$ is the sum of averaged lift power coefficients ($\bar{C}_{pl}$) and averaged moment power coefficients ($\bar{C}_{pm}$). $\bar{C}_x$ is averaged drag coefficients, which are used to understand the negative influence of α and β on performance of oscillating hydrofoils.

In Table. 2 η of flexure hydrofoils at α=5% and β=2.5 is 0.317, which is increase of about 17.8% compared to the rigid hydrofoil. As β increases, $\bar{C}_p$ and η is increased slightly. However, the increases are obviously with the increase of α from 0 to 15% at β=0.7 and further the increase is slightly as α from 15% to 20%. Furthermore, $\bar{C}_p$ and η are decreased gradually as increasing α from 20% to 30%. Similar tendency has been reported by Le et al [31], where efficiency increases from 38% (at A=0.15) to 39.2% (at A=0.2), while further increase A from 0.25 to 0.3 causes the decrease of efficiency from 39.8% to 39.6%.

It can be found in Table. 2 that the improvements of $\bar{C}_p$ are mainly attributed to the increase of $\bar{C}_{pl}$. It indicated that the power extraction depends on the heaving motion, which is consistent with Xie et al. [13]. However, it must be noted that with the increases of α and β, $\bar{C}_{pm}$ is increased, which means that the consumption of power is gradually increasing. In addition, $\bar{C}_x$ also increases with α and β increasing. Therefore, α=15% and β=1 is selected for further researches.

Table 2 Effect of α and β on $\bar{C}_p$ and η of hydrofoils.

α	β	$\bar{C}_x$	$\bar{C}_{pl}$	$\bar{C}_{pm}$	$\bar{C}_p$	η
0	0	0.931	0.711	-0.064	0.647	0.269
5%	0.7	1.107	0.799	-0.065	0.734	0.305
5%	1	1.115	0.809	-0.069	0.740	0.308
5%	1.5	1.133	0.821	-0.073	0.748	0.311
5%	2	1.149	0.832	-0.075	0.757	0.315
5%	2.5	1.175	0.841	-0.079	0.762	0.317

10%	0.7	1.266	0.853	-0.068	0.785	0.327
10%	1	1.297	0.868	-0.074	0.794	0.331
10%	1.5	1.312	0.879	-0.076	0.803	0.334
10%	2	1.347	0.901	-0.079	0.822	0.336
10%	2.5	1.359	0.912	-0.084	0.828	0.337
15%	0.7	1.396	0.967	-0.070	0.897	0.373
20%	0.7	1.798	0.998	-0.092	0.906	0.377
25%	0.7	1.913	0.992	-0.098	0.894	0.369
30%	0.7	2.218	0.987	-0.106	0.881	0.354

Variations of instantaneous lift and power coefficient with β are presented in Fig. 6. Lift coefficients (C_y) increase slightly with β increasing from 0.7 to 2.5 (Fig. 6(a)). However, C_y of all flexible cases (β=0.7-2.5) are larger than that of rigid hydrofoil (β=0). Fig. 6(b) shows the variation of C_p, which has the similar trend with Fig. 6(a).

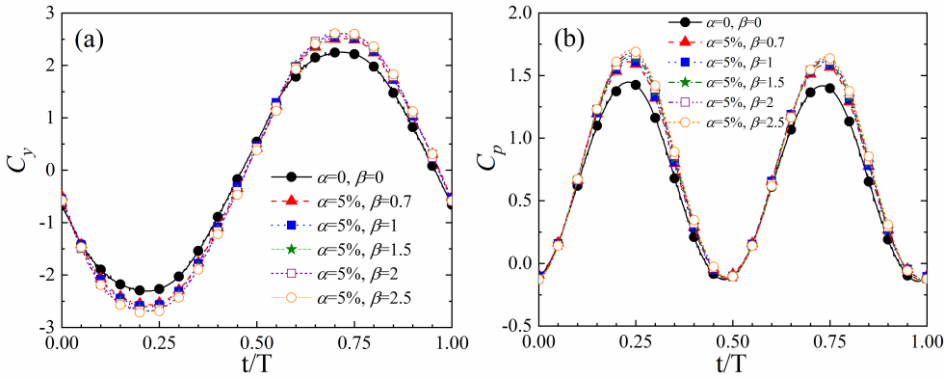

Fig. 6 Variations of C_y and C_p over one cycle for rigid hydrofoil (α=0 and β=0) and flexible hydrofoils (α=5% and β=0.7-2.5): (a) C_y and (b) C_p.

Fig. 7(a) shows the lift coefficient for different α varying from 0-20% at β=0.7. It can be seen that any increase in α causes to the increase of lift coefficients. The maximum lift coefficient is 3.21 at α=20% and t/T=0.2, which are approximately 40.2% higher than that of rigid hydrofoil (2.29). It can be seen in Fig. 7(b) and (c) that with the increase of α, C_x and C_m coefficients are increased, which increases the consumption of energy. Fig. 7(d) is provided to show the instantaneous power coefficient variation with α at fixed β=0.7. The instantaneous power coefficient increases obviously with α increasing from 5% to 20%. At t/T=0.23, maximum power coefficient of 2.04 is achieved, which is increase of about 40.6% as compared to the rigid hydrofoil (1.45).

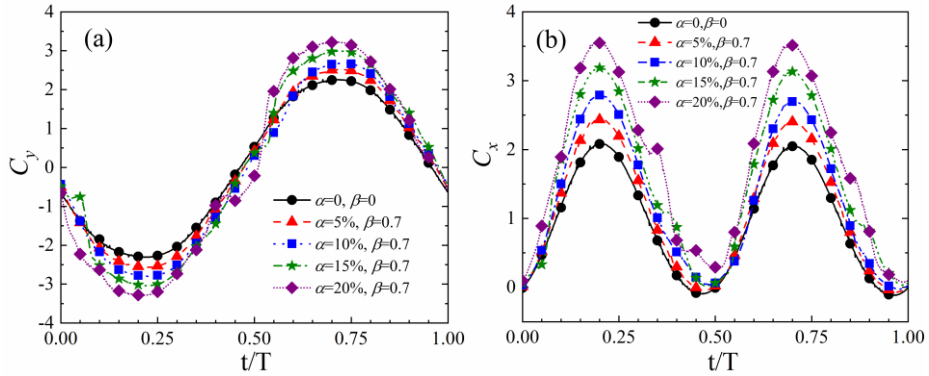

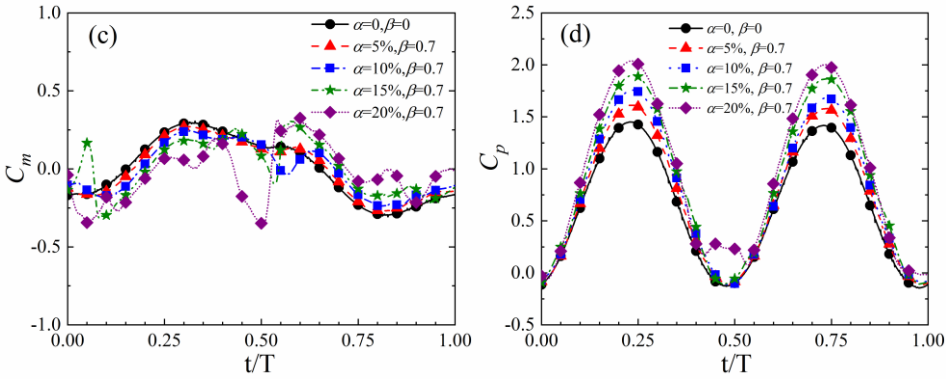

Fig. 7 The instantaneous force and power coefficient for rigid hydrofoil (α=0 and β=0) and flexible hydrofoil (α=5%-20% and β=0.7): (a) C_y, (b) C_x, (c) C_m, and (d) C_p.

According to Eq. (18), the power ($P(t)$) is positively related to force (F_y). What's more, there is a great correlation between force coefficients and the effective angle of attack (*AOA*). Therefore, the study of *AOA* can better understand the essence of the above phenomenon. Fig. 8(a) shows the *AOA* of α varying from 0-20%. As the increase of α, the *AOA* is gradually increased. Compared with α, the *AOA* cannot be changed obviously by the variation of β from 0.7 to 2.5 (Fig. 8(b)). It can be revealed that α can be used to alter the *AOA* of hydrofoils. Due to the *AOA* is less than the dynamic stall angle, the increase of *AOA* is beneficial for the improvement of C_y. Because h_0, θ_0 and f^* is constant, the heaving velocity and angular velocity are changeless. According to the equation (18), the increased C_y will improve the instantaneous power. Therefore, it can be determined that $\overline{C_p}$ and η are directly affected by the lift of hydrofoils, which depends on *AOA*.

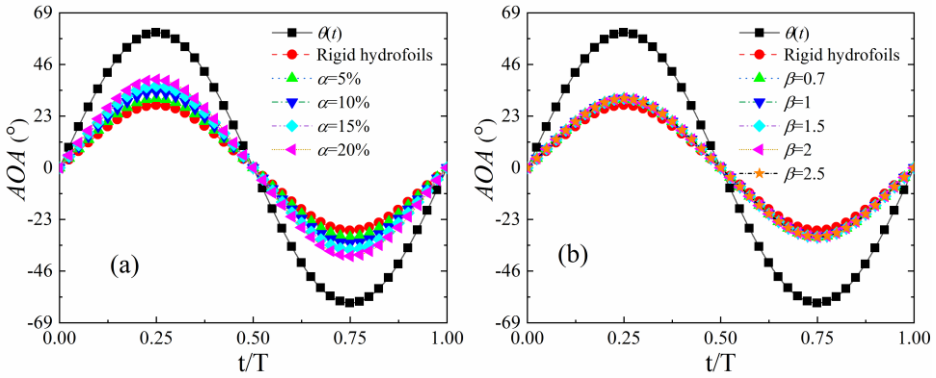

Fig. 8 the *AOA* of (a) α =5%-20% at β=0.7, and (b) β=0.7-2.5 at α =5%

3.3 Evolutions of pressure distribution and vortex field

From Eq. (10)-(12), it can be seen that C_y, C_x and C_m are subjected to the variation of forces, which are related to the pressure distribution of the surfaces on hydrofoils. Pressure distribution made a major contribution to force coefficients [10]. Therefore, observation of pressure distribution is necessary to analyze the effects of flexure parameters (α and β) on hydrodynamic performance.

It can be found in Fig. 9(a) that pressure difference mainly locates near the leading edge. In addition, the pressure difference of flexure hydrofoils (β=0.7-2.5) is very similar and greater than that of rigid hydrofoils (β=0).

The parameter α (5%, 10%, 15% and 20%) is equivalent to the maximum chordwise flexures of trailing edge tips respect to the chord length. It can be observed in Fig. 9(b) that the pressure difference of rigid hydrofoils (α=0) is smaller compared with flexible hydrofoils (α=5%-20%). With the increase of α, the pressure difference is increased gradually. It must be

noted that with α increasing, the projection distance on the x axis gradually approaches the origin, as marked by red arrows.

It can be seen in Fig. 9(a) and (b) that the pressure difference caused by larger α at fixed β is larger than that caused by varying β at fixed α. In other words, compared with adjusting β, adjusting α is more conducive to the increase of pressure difference. This indicated that more power can be extracted with a higher α.

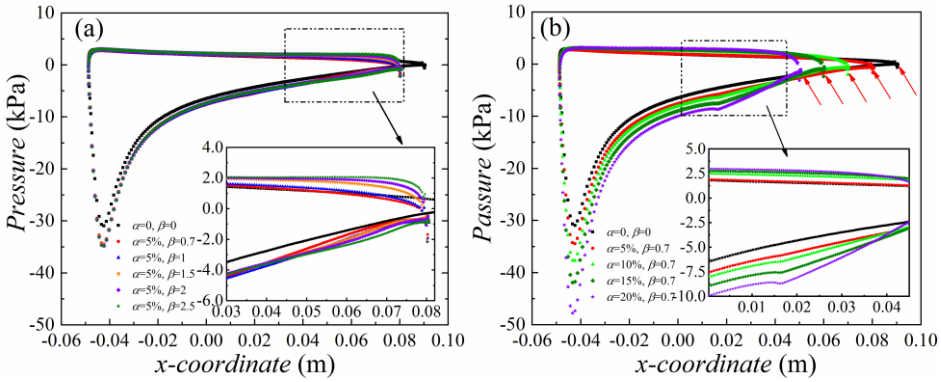

Fig. 9 Pressure distribution at t/T=0.2: (a) α=5%, β=0-2.5; (b) α=0-20%, β=0.7

Fig. 10 presents the vortex contours for different α varying from 0 to 20% at fixed β=0.7 during down-stroke phase. It must explain that up-stroke phase is the converse process of Fig. 10, and thus no exhibition in this section. At t/T=0, with α increase vortices are gradually generating. At t/T=0.15 the vortex is moving along the surface of hydrofoils. The pitch angle reaches peak values at t/T=0.25. However, when α increasing from 0 to 10%, boundary layer thickens gradually, which can be illustrated at t/T=0.25 and 0.35. The increase of α leads to reverse pressure gradient increasing greatly, which in return increases obviously boundary layer thickness. When α is greater than 10%, the boundary layer evolves into vortex at t/T=0.5. In addition, a second leading edge vortex can be found when α is greater than 15%, causing the fluctuation of lift coefficient. As shown in Fig. 10, no vortex is shedding away from near wall of hydrofoil, which means that no dynamic stall occurs.

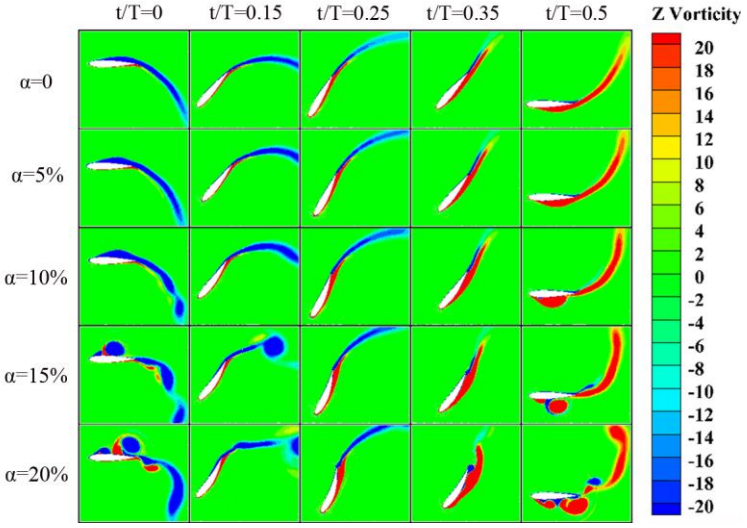

Fig. 10 Vortex contours at different moments for α=0-20%, β=0.7.

3.3 Influences of reduced frequency and pitching amplitude

The $\bar{C}_p$ for three modes (rigid hydrofoils, deformation mode 1 and mode 2) are shown in Fig. 11 at $0.025 \le f^* \le 0.325$, $40 \le \theta_0 \le 80$, α=15% and β=1. As shown in Fig. 11, the trend of $\bar{C}_p$

is increased firstly and then decreased under three modes. It indicates that a peak value of $\overline{C}_p$ exists in the range of f^* and θ_0. The peak value is gradually increased as f^* and θ_0 increases. The $\overline{C}_p$ of deformation mode 1 improved by approximately 55% compared with the rigid hydrofoil at f^*=0.175 and θ_0=70°. Interestingly, $\overline{C}_p$ of deformation mode 2 is lower than that of other types. Therefore, the deformation mode 2 can be used as adjustment measures in high velocity zone in order to protect turbines. This adjustment measure is carried out without stopping the machine, and the pressure on surface can be greatly reduced by simply changing the deformation mode.

In addition, for the different θ_0, there always exists a critical reduced frequency f^*_s. When $f^* < f^*_s$, $\overline{C}_p$ for three modes is very similar. However, when $f^* > f^*_s$, as f^* increase, the sensitivity of $\overline{C}_p$ is significantly increased. The f^*_s is generally increase with increasing θ_0.

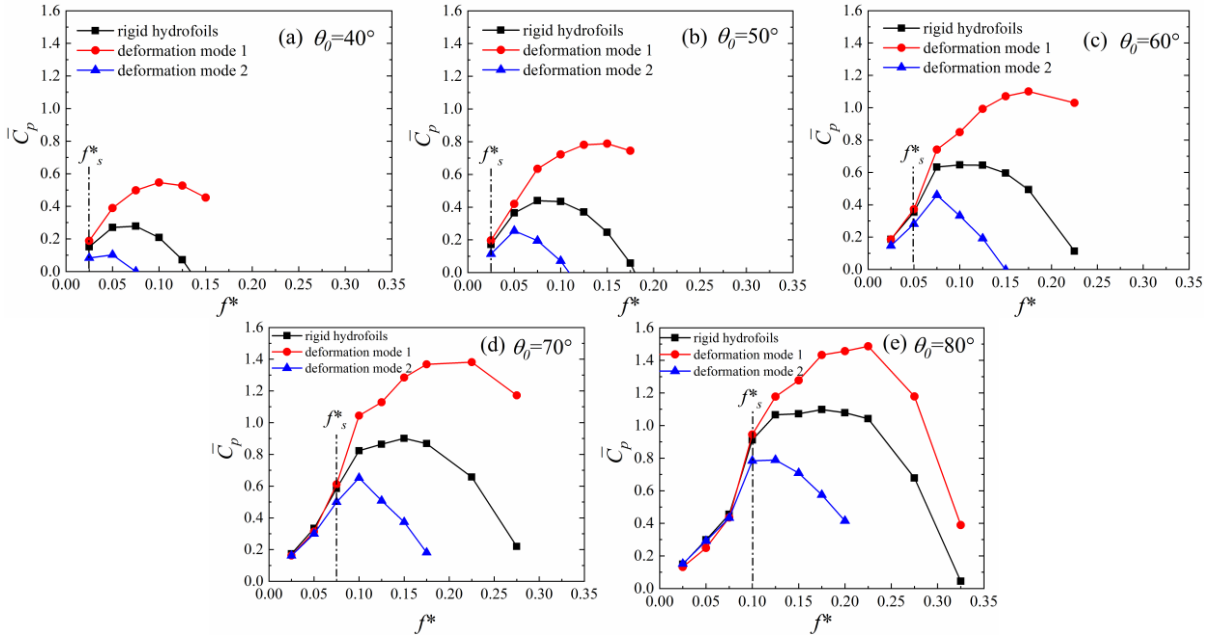

Fig. 11 The $\overline{C}_p$ for three modes (rigid hydrofoil, flexible deformation mode 1 and mode 2) at 0.025≤f^*≤0.325, 40≤θ_0≤80, α=15% and β=1.

To understand the influences of f^* on $\overline{C}_p$, f^* of 0.075, 0.175 and θ_0=80° are selected for further research. Fig. 12 exhibits C_y over one cycle for three modes.

As shown in Fig. 12 (a), C_y of deformation mode 1 is slightly large at 0-0.2t/T and 0.5-0.7t/T, however, the value is decrease seriously at 0.2-0.4t/T and 0.7-0.9t/T, resulting the limited difference of C_y in three modes. Therefore, $\overline{C}_p$ for three modes is very similar when $f^* < f^*_s$. Fig. 12(b) shows that when $f^* > f^*_s$, C_y of deformation mode 1 is the highest of the three in a period, resulting in a large difference of $\overline{C}_p$. In addition, the lift coefficient curve is relatively smooth, indicating that no stall has occurred.

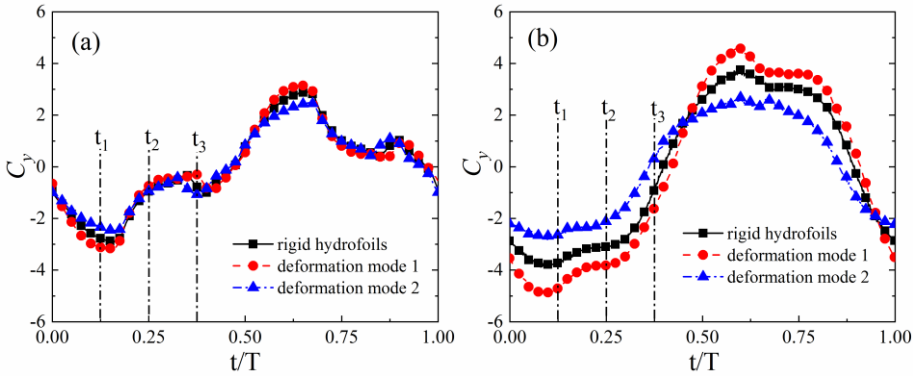

Fig. 12 The variation of instantaneous lift (C_y) over one cycle for three modes (a) f^*=0.075, (b) f^*=0.175.

Fig. 13 shows *AOA* over one cycle for three modes under f^*=0.075 and f^*=0.175 at θ_0=80°. From Fig. 13(a) and (b), *AOA* of deformation mode 1 is larger than that of rigid hydrofoils, which is consistent with Fig. 2(b). However, compared with rigid hydrofoils, deformation mode 2 decreases the *AOA* of hydrofoils.

At a low frequency (Fig. 13(a)), the corresponding heaving velocity is lower due to the same heaving amplitude, which leads to a lower induced velocity. According to the Eq. (6, 14-16), the decrease of an induced velocity increases the actual *AOA*. When the *AOA* is greater than the critical stall angle, hydrofoils will get into stall states, thus reducing C_y (Fig. 12(a)). Conversely, at a high frequency (Fig. 13(b)), *AOA* is decreased due to the increase of induced velocities. Therefore, C_y (Fig. 12(b)) keeps a large value for a long time, which is beneficial for the improvement of $\overline{C_p}$.

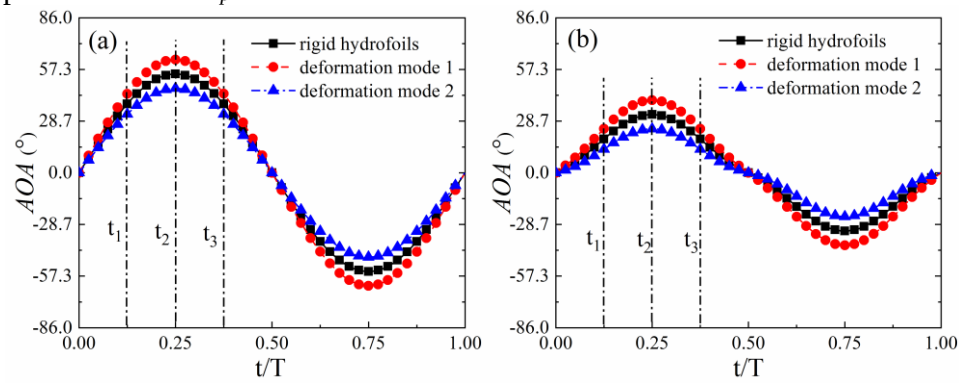

Fig. 13 *AOA* over one cycle for three modes (a) f^*=0.075, (b) f^*=0.175.

Fig. 14 shows the vortex contours for f^*=0.075 and f^*=0.175. It can be seen in Fig. 14(a) that from t/T=0 to t_1, boundary layer separation does not occur, and the lift coefficient increases steadily, but vortex separation occurs at t/T=t_2 stage, resulting in a serious drop in lift coefficient. This corresponds to the lift curve in Fig. 12(a) above. At t/T=t_3 stage, the vortex is shedding away from the surface of hydrofoils and interacting with the wake vortex.

As shown in Fig.14(b), no leading-edge vortex sheds in the whole cycle, which means that there is no stall occurring. The lift coefficient curve transitions smoothly, which corresponds to the lift coefficient curve (Fig. 12(b)). By comparing the three modes, it can be seen that deformation mode 1 has some degree of stall delay, which can be illustrated at t/T=0-t_3. In addition, deformation mode affects the motion state of the fluid near the lower surfaces at down-stroke. Under the deformation mode 1, because the flexure direction is the same as the pitching direction, an anticlockwise direction vortex near the trailing edge (t/T=t_2), which caused by pitching motion, is strengthened by deformation movement. The vortex will lead to the separation of the boundary layer. For comparison, due to the flexure direction is opposite to the pitching direction under deformation mode 2, the deformation motion weakens the vortex caused by pitching motion, which leads to the fluid being closer to the lower surfaces at down-stroke.

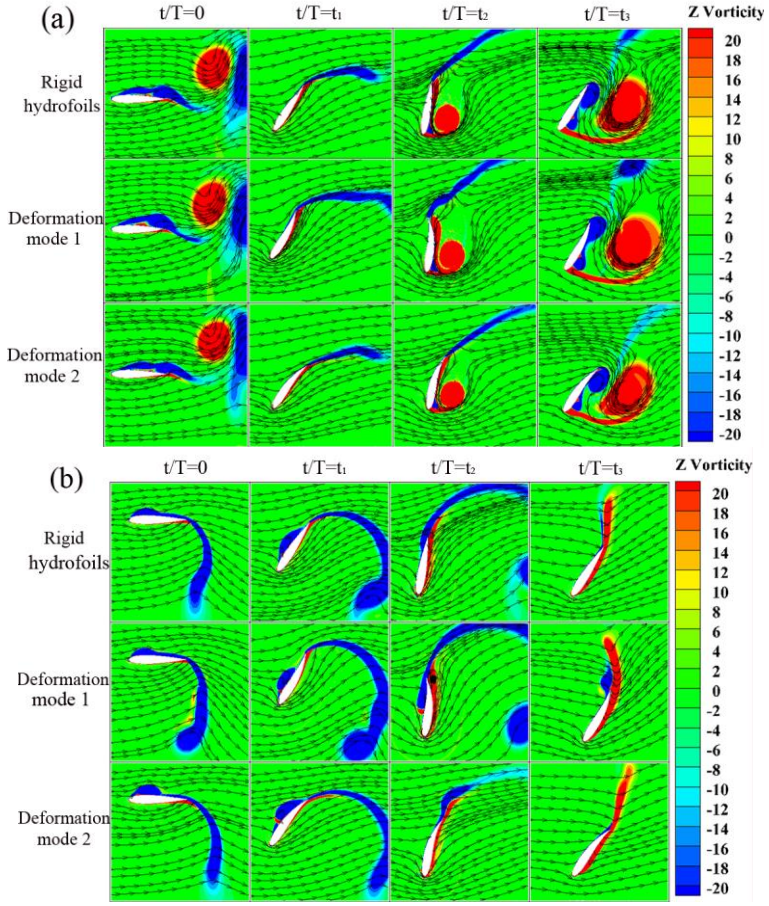

Fig. 14 Vortex contours of (a) f^*=0.075, (b) f^*=0.175.

It can be seen in Fig. 15(a) that at lower f^* the pressure difference in three modes is very similar, which leads to a limited difference in lift coefficient (Fig. 12(a)). However, the pressure difference of deformation mode 1 is larger than that of rigid hydrofoil and deformation mode 2 at higher f^* (Fig. 15(b)), resulting the higher lift coefficient (Fig. 12(b)).

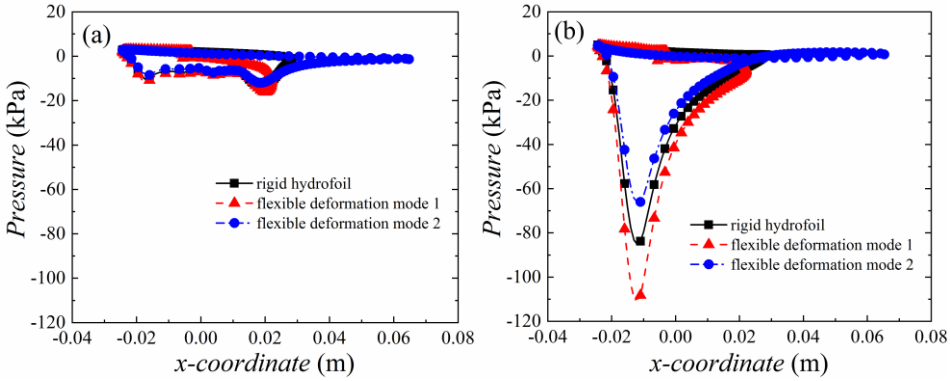

Fig. 15 Pressure distribution at t/T=t2 of (a) f^*=0.075, (b) f^*=0.175.

As shown in Fig. 16(a), the peak η of 41% and the zone of high η (34.2%<η<41%) were achieved at 0.1<f^*<0.175 and 65°<θ_0<80°. The highest η of deformation mode 1 was up to 54.3% and the zone of high η (36.1%<η<54.3%), which is at 0.1<f^*<0.25 and 55°<θ_0<80°, is wider than that of rigid hydrofoils. However, compared with the rigid hydrofoil and deformation mode 1, the deformation mode 2 have a lower peak η of 30.3% and a narrower zone of high η (26.9%<η<30.3%) at 0.075<f^*<0.15 and 70°<θ_0<80°. It can be inferred that the deformation mode 2 has obvious effects on reducing power-extraction efficiency without

changing f^* and θ_0.

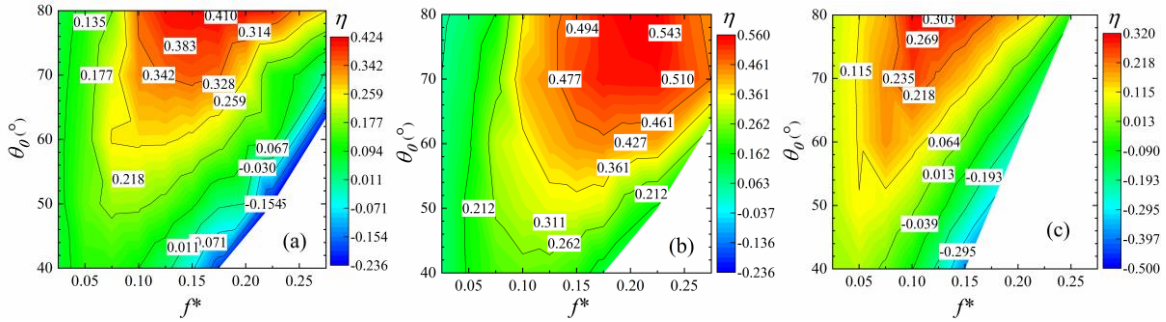

Fig. 16 η for three modes: (a) rigid hydrofoils, (b) deformation mode 1 and (c) deformation mode 2

4. Conclusions

In this study, the effects of α, β , f^*, θ_0 and deformation modes on energy extraction capacity of a flexible hydrofoil were investigated using the commercially available software Fluent. The results are as follows:

(1) Energy extraction capacity is affected seriously by the chordwise flexibility. Power coefficients and efficiency are sensitive to α, while the influences of flexible coefficient β are very limited. In addition, $\bar{C}_p$ and η are increased obviously with α increasing from 0 to 15%, while the increase of them is very limited as α further increase from 15% to 20%. As α increase from 0 to 10%, boundary layer thickens, while a leading-edge vortex shedding along the near wall to the trailing edge when α further increase from 10% to 20%.

(2) Flexible deformation modes affect *AOA* and vortex structure, which alter the pressure difference, and thus affect the power extraction capacity. The order of power extraction capacity is: deformation mode 1 > rigid hydrofoils > deformation mode 2.

(3) Interestingly, there is a critical reduced frequency f^*_s under three modes, when $f^* < f^*_s$, $\bar{C}_p$ for three modes is very similar; However, when $f^* > f^*_s$, as f^* increase, the sensitivity of $\bar{C}_p$ is significantly increased. In addition, the f^*_s is generally increase with increasing θ_0. Therefore, the adjustment of flexure modes and parameters, which is made according to different requirement of power coefficient under different tidal currents, should be carried out under the condition that f^* is larger than f^*_s.

(4) The order of peak η of three modes is: deformation mode 1 (54.3%) > rigid hydrofoils (41%) > deformation mode 2 (30.3%); And the range of high η is: deformation mode 1 ($36.1\% < \eta < 54.3\%$) > rigid hydrofoils ($34.2\% < \eta < 41\%$) > deformation mode 2 ($26.9\% < \eta < 30.3\%$).

The interaction between the flexible hydrofoil and the fluid flow in the real tidal currents is complicated. The fluid-structure interaction can be calculated by a fully two-way coupling approach [40-42]. In the future, this approach should be used for the simulation of the flexible hydrofoil.

ACKNOWLEDGMENTS

This work was supported by the National Natural Science Foundation of China [No. 51875316] and the Natural Science Foundation of Shandong Province [ZR2019MEE025].

REFERENCES

[1] Segura, E., Morales, R., Somolinos, J. A, Lopez, A., 2017. Techno-economic challenges of tidal energy conversion systems: Current status and trends. *Renewable and Sustainable Energy Reviews*, 77, 536-550. http://dx.doi.org/10.1016/j.rser.2017.04.054

[2] McKinney, W., DeLaurier, J., 1981. Wingmill: An Oscillating-Wing Windmill. *Journal of Energy*, 5(2): 109-115. https://doi.org/10.2514/3.62510

[3] Young, J., Lai, J. C. S., Platzer, M. F., 2014. A review of progress and challenges in flapping foil power generation. *Progress in Aerospace Sciences*, 67, 2-28. http://dx.doi.org/10.1016/j.paerosci.2013.11.001

[4] Kinsey, T., Dumas, G., 2012. Computational fluid dynamics analysis of a hydrokinetic turbine based on oscillating hydrofoils. *Journal of Fluids Engineering*, 134(2), 021104. https://doi.org/10.1115/1.4005841

[5] Kinsey, T., Dumas, G., 2008. Parametric Study of an Oscillating Airfoil in a Power-Extraction Regime. *AIAA Journal*, 46(6), 1318-1330. https://doi.org/10.2514/1.26253

[6] Zhu, Q., Peng, Z. 2009. Mode coupling and flow energy harvesting by a flapping foil. *Physics of Fluids*, 21(3), 033601. https://doi.org/10.1063/1.3092484

[7] Xiao, Q., Zhu, Q., 2014. A review on flow energy harvesters based on flapping foils. *Journal of Fluids and Structures*, 46, 174-191. https://doi.org/10.1016/j.jfluidstructs.2014.01.002

[8] Young, J., Lai, J. C. S., 2004. Oscillation Frequency and Amplitude Effects on the Wake of a Plunging Airfoil. *AIAA Journal*, 42(10), 2042-2052. https://doi.org/10.2514/1.5070

[9] Kinsey, T., Dumas, G., 2014. Optimal Operating Parameters for an Oscillating Foil Turbine at Reynolds Number 500,000. *AIAA Journal*, 52(9), 1885-1895. https://doi.org/10.2514/1.J052700

[10] Xiao, Q., Liao, W., Yang, S., Peng, Y., 2012. How motion trajectory affects energy extraction performance of a biomimic energy generator with an oscillating foil?. *Renewable Energy*, 37(1), 61-75. https://doi.org/10.1016/j.renene.2011.05.029

[11] Lu, K., Xie, Y., Zhang, D., 2014. Nonsinusoidal motion effects on energy extraction performance of a flapping foil. *Renewable Energy*, 64, 283-293. https://doi.org/10.1016/j.renene.2013.11.053

[12] Ashraf, M. A., Young, J., Lai, J. C. S., Platzer, M. F., 2011. Numerical Analysis of an Oscillating-Wing Wind and Hydropower Generator. *AIAA Journal*, 49(7), 1374-1386. https://doi.org/10.2514/1.J050577

[13] Xie, Y., Lu, K., Zhang, D., 2014. Investigation on energy extraction performance of an oscillating foil with modified flapping motion. *Renewable Energy*, 63, 550-557. https://doi.org/10.1016/j.renene.2013.10.029

[14] Ma, P., Wang, Y., Xie, Y., Zhang, J., 2018. Analysis of a hydraulic coupling system for dual oscillating foils with a parallel configuration. *Energy*, 143, 273-283. https://doi.org/10.1016/j.energy.2017.10.141

[15] Ma, P., Wang, Y., Xie, Y., Huo, Z., 2018. Numerical analysis of a tidal current generator with dual flapping wings. *Energy*, 155, 1077-1089. https://doi.org/10.1016/j.energy.2018.05.035

[16] Karbasian, H. R., Esfahani, J. A., Barati, E., 2015. Simulation of power extraction from tidal currents by flapping foil hydrokinetic turbines in tandem formation. *Renewable Energy*, 81, 816-824. https://doi.org/10.1016/j.renene.2015.04.007

[17] Xu, J., Sun, H., Tan, S., 2016. Wake vortex interaction effects on energy extraction performance of tandem oscillating hydrofoils. *Journal of Mechanical Science and Technology*, 30(9), 4227-4237. https://doi.org/10.1007/s12206-016-0835-9

[18] Kim, J., Quang Le, T., Hwan Ko, J., Sitorus, P. E., Tambunan, I. H., Kang, T., 2015. Experimental and numerical study of a dual configuration for a flapping tidal current generator. *Bioinspiration & Biomimetics*, 10(4), 046015. https://doi.org/10.1088/1748-3190/10/4/046015

[19] Ma, P., Yang, Z., Wang, Y., Liu, H., Xie, Y., 2017. Energy extraction and hydrodynamic behavior analysis by an oscillating hydrofoil device. *Renewable Energy*, 113, 648-659. https://doi.org/10.1016/j.renene.2017.06.036

[20] Sitorus, P. E., Ko, J. H., 2019. Power extraction performance of three types of flapping hydrofoils at a Reynolds number of 1.7E6. *Renewable Energy*, 132, 106-118. https://doi.org/10.1016/j.renene.2018.07.116

[21] Karbasian, H. R., Esfahani, J. A., Barati, E., 2016. The power extraction by flapping foil hydrokinetic turbine in swing arm mode. *Renewable Energy*, 88, 130-142. https://doi.org/10.1016/j.renene.2015.11.038

[22] Lahooti, M., Kim, D., 2019. Multi-body interaction effect on the energy harvesting performance of a flapping hydrofoil. *Renewable Energy*, 130, 460-473. https://doi.org/10.1016/j.renene.2018.06.054

[23] Ma, P., Wang, Y., Xie, Y., Huo, Z., 2018. Effects of time-varying freestream velocity on energy harvesting using an oscillating foil. *Ocean Engineering*, 153, 353-362. https://doi.org/10.1016/j.oceaneng.2018.01.115

[24] Wang, Y., Sun, X., Huang, D., Zheng, Z., 2016. Numerical investigation on energy extraction of flapping hydrofoils with different series foil shapes. *Energy*, 112, 1153-1168. https://doi.org/10.1016/j.energy.2016.06.092

[25] Shin, S., Bae, S. Y., Kim, I. C., Kim, Y. J., 2009. Effects of flexibility on propulsive force acting on a heaving foil. *Ocean Engineering*, 36(3-4), 285-294. https://doi.org/10.1016/j.oceaneng.2008.12.002

[26] Zhu, Q., 2007. Numerical Simulation of a Flapping Foil with Chordwise or Spanwise Flexibility. *AIAA Journal*, 45(10), 2448-2457. https://doi.org/10.2514/1.28565

[27] Tay, W. B., Lim, K. B., 2010. Numerical analysis of active chordwise flexibility on the performance of non-symmetrical flapping airfoils. *Journal of Fluids and Structures*, 26(1), 74-91. https://doi.org/10.1016/j.jfluidstructs.2009.10.005

[28] Jeanmonod, G., Olivier, M., 2017. Effects of chordwise flexibility on 2D flapping foils used as an energy extraction device. *Journal of Fluids and Structures*, 70, 327-345. https://doi.org/10.1016/j.jfluidstructs.2017.01.009

[29] Tian, F. B., Young, J., Lai, J. C. S., 2014. Improving power-extraction efficiency of a flapping plate: From passive deformation to active control. *Journal of Fluids and Structures*, 51, 384-392. https://doi.org/10.1016/j.jfluidstructs.2014.07.013

[30] Liu, Z., Tian, F. B., Young, J., Lai, J. C. S., 2017. Flapping foil power generator performance enhanced with a spring-connected tail. *Physics of Fluids*, 29(12), 123601. https://doi.org/10.1063/1.4998202

[31] Le, T. Q., Ko, J. H., 2015. Effect of hydrofoil flexibility on the power extraction of a flapping tidal generator via two- and three-dimensional flow simulations. *Renewable Energy*, 80, 275-285. https://doi.org/10.1016/j.renene.2015.01.068

[32] Wu, J., Wu, J., Tian, F.B., Zhao, N., Li, Y. D., 2015. How a flexible tail improves the power extraction efficiency of a semi-activated flapping foil system: A numerical study. *Journal of Fluids and Structures*, 54, 886-899. https://doi.org/10.1016/j.jfluidstructs.2015.02.006

[33] Wu, J., Shu, C., Zhao, N., Tian, F. B. 2015. Numerical study on the power extraction performance of a flapping foil with a flexible tail. *Physics of Fluids*, 27(1), 013602. https://doi.org/10.1063/1.4905537

[34] Siala, F. F., Kamrani Fard, K., Liburdy, J. A., 2020. Experimental study of inertia-based passive flexibility of a heaving and pitching airfoil operating in the energy harvesting regime. *Physics of Fluids*, 32(1), 017101. https://doi.org/10.1063/1.5119700

[35] Totpal, A. D., Siala, F. F., Liburdy, J. A., 2018. Energy harvesting of an oscillating foil at low reduced frequencies with rigid and passively deforming leading edge. *Journal of Fluids and Structures*, 82, 329-342. https://doi.org/10.1016/j.jfluidstructs.2018.04.022

[36] Zhu, B., Xia, P., Huang, Y., Zhang, W., 2019. Energy extraction properties of a flapping wing with an arc-deformable airfoil. *Journal of Renewable and Sustainable Energy*, 11(2), 023302. https://doi.org/10.1063/1.5079864

[37] Kinsey, T., Dumas, G., Lalande, G., Ruel, J., Mehut, A., Viarouge, P., Lemay, J., Jean, Y., 2011. Prototype testing of a hydrokinetic turbine based on oscillating hydrofoils. *Renewable Energy*, 36(6), 1710-1718. https://doi.org/10.1016/j.renene.2010.11.037

[38] Bose, N., 1995. Performance of chordwise flexible oscillating propulsors using a time-domain pan method. *International Shipbuilding Progress*, 42(432), 281-294. 10.3233/ISP-1995-4243201

[39] Ma, P., Wang, Y., Xie, Y., Han, J., Sun, G., Zhang, J., 2019. Effect of wake interaction on the response of two tandem oscillating hydrofoils. *Energy Science & Engineering*, 7(2), 431-442. https://doi.org/10.1002/ese3.286

[40] Tuković, Ž., Karač, A., Cardiff, P., Jasak, H., Ivanković, A., 2018. OpenFOAM finite volume solver for fluid-solid interaction. *Transactions of FAMENA*, 42(3), 1–31. https://doi.org/10.21278/TOF.42301

[41] Huang, L., Ren, K., Li, M., Tuković, Ž., Cardiff, P., Thomas, G., 2019. Fluid-structure interaction of a large ice sheet in waves. *Ocean Engineering*, 182, 102–111. https://doi.org/10.1016/j.oceaneng.2019.04.015

[42] Huang, L., Li, Y., 2021. Design of the submerged horizontal plate breakwater using a fully coupled hydroelastic approach. *Computer-Aided Civil and Infrastructure Engineering*, Online first https://doi.org/10.1111/mice.12784

Submitted: 17.12.2021.
Accepted: 21.02.2022.

Yubing Zhang[a]
Yong Wang[a, b, *], meywang@sdu.edu.cn
Guang Sun[a]
Jiazhen Han[a]
Yudong Xie[a, *], ydxie@sdu.edu.cn
[a] School of Mechanical Engineering, Shandong University, Jinan, Shandong 250061, China
[b] Key Laboratory of High-efficiency and Clean Mechanical Manufacture, Shandong University, Ministry of Education, Jinan, Shandong 250061, China
* Corresponding author: Yong Wang, Yudong Xie